European Journal of Mechanics / A Solids 103 (2024) 105156

Contents lists available at ScienceDirect

European Journal of Mechanics / A Solids

journal homepage: www.elsevier.com/locate/ejmsol

Failure of topologically interlocked structures — a Level-Set-DEM approach

Shai Feldfogel [a], Konstantinos Karapiperis [b], Jose Andrade [c], David S. Kammer [a,*]

[a] Institute for Building Materials, ETH Zurich, Switzerland
[b] Department of Mechanical and Process Engineering, ETH Zurich, Switzerland
[c] Department of Mechanical and Civil Engineering, Caltech, Pasadena, CA, USA

ARTICLE INFO

Keywords:
Topologically interlocked structures
Level-set
Discrete-element model

ABSTRACT

Topological Interlocking Structures (TIS) are assemblies of interlocking building blocks that hold together solely through contact and friction at the block interfaces and thus do not require any connective elements. This salient feature makes them highly energy-absorbent, resistant to crack propagation, geometrically versatile, and reusable. It also gives rise to failure mechanisms that, differently from ordinary structures, are governed by multiple contact interactions between blocks and frictional slip at their interfaces. Commonly-used modeling tools for structural analysis struggle to capture and quantify these unusual failure mechanisms. Here, we propose a different approach that is well-suited for modeling the complex failure of slab-like TIS. It is based on the Level-Set-Discrete-Element-Method, which was originally developed for granular mechanics applications. After introducing the basic assumptions and theoretical concepts underlying our model, we show that it accurately captures the slip-governed failure of slab-like TIS panels as observed in the literature, that it can closely estimate the force–displacement curves, and that it is can be used to explore important features governing the structural mechanics of TIS. The theoretical foundation, together with the results of this study, provide a proof-of-concept for our new approach and point to its potential to improve our ability to model and understand the behavior of interlocked structural forms.

1. Introduction

Topological Interlocking Structures (TIS) are assemblies of interlocking building blocks that hold together solely through contact and friction at the block interfaces and thus do not require any connective elements, see Fig. 1 left. This defining feature sets them apart from ordinary structural forms and it is responsible for their unique behavior and advantageous properties (Dyskin et al., 2005; Molotnikov et al., 2007; Carlesso et al., 2012, 2013; Dyskin et al., 2019, 2012). In spite of their attractive properties, TIS' promising potential is yet to translate to large-scale prevalence, likely because our ability to predict their failure – a prerequisite for designing them safely – is far from fully developed.

Developing predictive capabilities for the behavior and failure of TIS is challenging because TIS blocks are not connected by any mechanical means (e.g., adhesives or bolts) and the structural integrity therefore relies on transmission of forces through the interfaces. These interfacial forces are difficult to quantify and predict because the interfacial contact conditions that govern them are: (a) geometrically irregular and dynamically changing by nature (Djumas et al., 2017); (b) highly dependent on local slip failures (Djumas et al., 2017; Mirkhalaf et al., 2019; Koureas et al., 2022); (c) coupled with all other interfaces through the global response; and (d) sensitive to unavoidable geometrical imperfections (Mirkhalaf et al., 2019; Barthelat and Zhu, 2011).

As shown ahead, commonly-used models struggle to capture and quantify the slip-governed failure of TIS, pointing to the potential benefit of alternative modeling approaches. The main aim of this study is to establish a proof-of-concept for a new computational approach, one based on applying the Level-Set-Discrete-Element-Method (LS-DEM), originally developed for granular applications, to structural analysis of TIS, see Fig. 1.

The most commonly-used tool to model the behavior and failure of TIS is the Finite Element Method (FEM), see Williams and Siegmund (2021), Short and Siegmund (2019), Djumas et al. (2017), Mirkhalaf et al. (2019), Schaare et al. (2008), Dalaq and Barthelat (2020) and Dalaq and Barthelat (2019). This is a natural choice due to FEM's ability to handle arbitrarily shaped solids and to accurately resolve their stress and deformation fields. In cases where the response was entirely governed by a stick regime and the specimens were not loaded up to failure, FEM obtained a very good agreement with experimental and analytical results (Schaare et al., 2008; Short and Siegmund, 2019). In the context of beam-like assemblies with few blocks, FEM was also able to correctly capture the experimentally-observed slip-governed failure

* Corresponding author.
E-mail address: dkammer@ethz.ch (D.S. Kammer).

https://doi.org/10.1016/j.euromechsol.2023.105156
Received 4 October 2022; Received in revised form 15 September 2023; Accepted 6 October 2023
Available online 10 October 2023

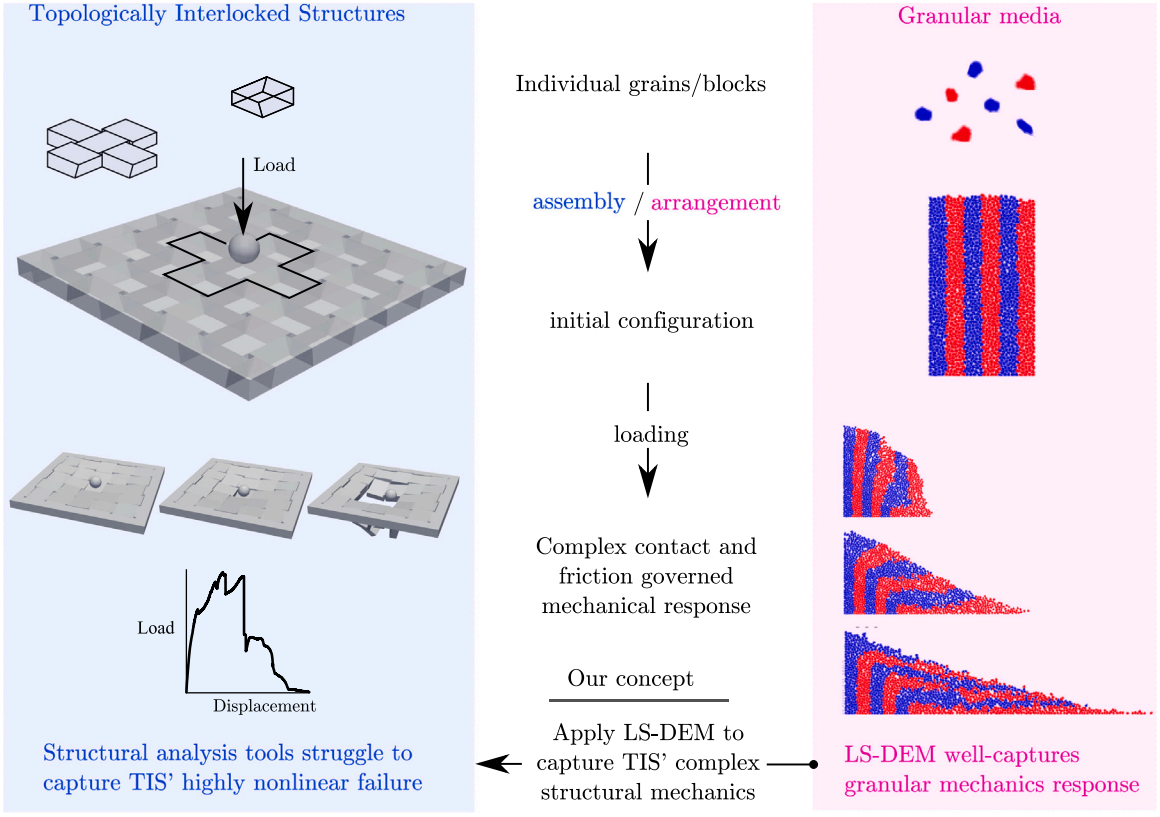

Fig. 1. Illustration of presented concept: Based on the similarities between TIS and granular media on the one hand, and LS-DEM unique ability to model the latter's mechanics on the other, we apply LS-DEM to model the complex failure of TIS, which common structural analysis tools struggle to capture.

mechanism and match well the global load displacement curves (Dalaq and Barthelat, 2020). However, as stated in Dalaq and Barthelat (2020), computational-cost issues arise when modeling TIS with more than a few blocks using FEM, and this becomes problematic in the context of slab-like TIS, which typically comprise dozens of blocks.

In spite of the computational challenges that the slip-governed behavior of slab-like TIS poses, FEM has been able to correctly capture and quantify experimentally-observed slip-governed failure of a dynamically-loaded TIS panel made of tetrahedral blocks (Feng et al., 2015). This required calibrating two parameters — the contact stiffness k_n and the friction coefficient μ. Reasonable agreement was also obtained in Rezaee Javan et al. (2017) in terms of the load–deflection curves of dynamically-loaded TIS panels, but the failure mechanism predicted by FEM were not shown. The most computationally challenging context is, arguably, the quasi-static regime. This is expressed, for example, by large over-prediction of the peak load (Mirkhalaf et al., 2019) and by divergence of the analyses from the experimental results close to failure (Djumas et al., 2017).

The Discrete Element Method (DEM) was originally designed to model dynamically-evolving contact and friction interactions between multiple spherical grains (Cundall and Strack, 1979). It relies on an explicit dynamic framework, a rigid-body assumption, elementary block shapes (mostly spherical, and generally convex), and a penalty-enforced contact between the blocks, properties that make it a natural framework to addressing the intricate behavior and failure of TIS.

DEM's potential for TIS is, curiously, supported by Schaare et al. (2008), where excellent agreement with experimental results was obtained using extremely coarse FEM meshes with only 8 elements per block (three orders of magnitude less than in Djumas et al. (2017)). This suggests that a coarse representation of block deformation, one that is also possible in DEM as will be explained ahead, may suffice to capture the essential features in TIS' structural response.

DEM was used by Brugger et al. (2008, 2009) to model centrally loaded slab-like TIS with cube shaped blocks, but this approach has not been further explored. The limiting element in DEM as a general modeling approach to TIS is the lack of geometrical generality necessary to fully address the variety of TI blocks and their complex contacts.

Recently, a geometrically versatile DEM variant called Level-Set-DEM (LS-DEM) (Kawamoto et al., 2016) was developed. LS-DEM is able to represent arbitrary block geometries and resolve the complex contact kinematics that arise between them through a node-based discretization of block boundary. This makes LS-DEM a potentially attractive approach for TIS, see Fig. 1-right and Karapiperis et al. (2022). Recently, LS-DEM's original contact formulation has been adapted, enabling us to use it for structural analysis (Feldfogel et al., 2022). However, LS-DEM ability to realistically capture and predict the behavior and failure of TIS as observed in experiments – a necessary validation test for a model – has not yet been established.

Summarizing, efficient and reliable computational tools are indispensable to modeling the slip-governed failure of TIS. Yet, capturing this complex phenomenon still poses major modeling and computational challenges to FEM and DEM alike. The main objectives of this manuscript are to present the concepts underlying LS-DEM as a computational model for TIS and to show that it is a viable and useful modeling alternative

2. Methodology

2.1. Assumptions

The modeling assumptions underlying our LS-DEM model involve global considerations, the blocks, and the interfaces. Globally, the structural response is defined by the 3D rigid body motions of the blocks, which are governed by Newton's generalized laws of motion. Accordingly, the total number of degrees of freedom equals the number

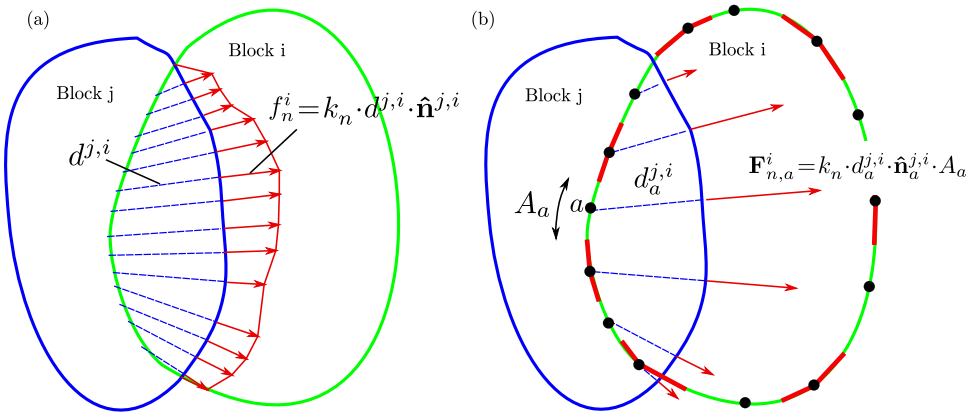

Fig. 2. Contact modeling — (a) the continuum-based approach; and (b) LS-DEM's discretized nodal forces (penetrations are grossly exaggerated for illustrative purposes).

of blocks times six (the number of rigid body degrees of freedom), and it is smaller by three orders of magnitude compared to FEM models reported in the literature, see, e.g. Djumas et al. (2017). The energy dissipation mechanisms comprise sliding friction, restitution losses, and global damping.

The blocks are assumed to be unbreakable rigid bodies; their mass corresponds to their true material density (no mass scaling); and the forces acting on them comprise gravity, contact and friction interface forces by adjacent blocks, support reactions by Dirichlet boundaries, and damping forces.

The interfaces are assumed to be adhesion-less, so only normal compressive forces and tangential friction forces are considered; contact is enforced in a linear-penalty sense. A regularized Coulomb law is adopted, whereby the shear traction is given as:

$$\boldsymbol{\tau} = \frac{\Delta \boldsymbol{s}}{\|\Delta \boldsymbol{s}\|} \min(k_t \|\Delta \boldsymbol{s}\|, \mu \|\boldsymbol{\sigma}\|) \tag{1}$$

where k_t denotes a shear penalty parameter with units of traction per unit displacement, analogously to k_n, μ is the friction coefficient, with no distinction being made between static and kinetic friction, and $\boldsymbol{\sigma}$ is the normal traction at the contact region.

2.2. Mathematical formulation

The mathematical formulation of LS-DEM has been detailed elsewhere (Kawamoto et al., 2016; Feldfogel et al., 2022) and it is not repeated here in full for the sake of brevity. Nevertheless, the adapted contact formulation introduced in Feldfogel et al. (2022) and adopted here is briefly described for completeness.

As illustrated in Fig. 2(a), we adopt a continuum-based contact approach wherein contacting block surfaces are thought of as elastic foundations, exerting equal and opposite normal compressive tractions f_n^i proportional to the penetrations $d^{j,i}$ at each contact point. Accordingly, the penetration stiffness k_n has dimensions of traction per unit penetration and it is analogous to the elastic foundation modulus.

In LS-DEM, the block surfaces are discretized by seeding nodes across them, as schematically shown on block i in Fig. 2(b). Accordingly, the continuous contact tractions in Fig. 2(a) are represented by discrete nodal forces, shown as red arrows in Fig. 2(b). The nodal force $\mathbf{F}_{n,a}^i$ at contact node a reads[1]:

$$\mathbf{F}_{n,a}^i = k_n \cdot d_a^{j,i} \cdot \hat{\mathbf{n}}_a^{j,i} \cdot A_a \tag{2}$$

where the subscript a represent the a'th contact node and where A_a is the nodal tributary area. Note that the method allows for robust treatment of corners, as encountered at the edges of blocks. This is due to the computation of normals (gradients of the level set function) by means of trilinear interpolation from the nearest points in the level set grid. The interested reader is referred to Kawamoto et al. (2016) for more details.

2.3. Modeling deformability with rigid blocks

Under the rigid body assumption used in LS-DEM, it is not possible to directly account for the in-plane deformability of the blocks, which governs the stiffness and capacity of TIS. Instead, we account for this deformability indirectly through the block penetrations and the commensurate penetration stiffness k_n, as explained next.[2]

Beginning with the simple case of two-blocks of total length L under in-plane compressive traction σ depicted in Fig. 3(a), the total shortening is the sum of elastic shortenings of the blocks $\Delta = \frac{\sigma \cdot L}{E}$, see Fig. 3(b). In models where contact between deformable blocks is imposed in a penalty sense (one of the two most popular approaches in FEM, alongside the more accurate Lagrange multiplier methods), the total shortening depicted in Fig. 3(c) is the sum of the elastic deformations and the interface penetration thus $\Delta_{FEM} = \frac{\sigma \cdot L}{E} + \frac{\sigma}{k_n}$. In our LS-DEM model, the total shortening depicted in Fig. 3(d) equals the interface penetration $\Delta_{LSDEM} = \frac{\sigma}{k_n}$. By equating Δ_{LSDEM} to Δ and solving for k_n we obtain $k_n = k_n^{def} = \frac{E}{L}$, a value that yields the same elastic shortening and therefore the same effective in-plane deformability. In this simplified approach, k_n has a dual function of penetration stiffness and a correlate of the elastic modulus.

In assemblies with $M+1$ blocks, see Fig. 3(e), the total shortening is again $\Delta = \frac{\sigma \cdot L}{E}$, Fig. 3(f), but $\Delta_{LSDEM} = \sum \frac{\sigma}{k_n} = M \cdot \frac{\sigma}{k_n}$, where M is the number of interfaces across which penetrations occur, Fig. 3(g). Equating Δ and Δ_{LSDEM} and solving for k_n yields the general closed-form expression:

$$k_n = k_n^{def} = \frac{M \cdot E}{L} \tag{3}$$

[1] To avoid redundant symbols, k_n^* from Feldfogel et al. (2022) has been denoted here by k_n, with the understanding that its dimension is still traction per unit displacement and not force per unit displacement as in the original LS-DEM formulation.

[2] It is tacitly assumed in the following derivation that the in-plane action is the most dominant factor governing the response of TIS panels and that the effects of shear deformations can be neglected as secondary. This approach follows the thrust-line model (Krause et al., 2012; Khandelwal et al., 2013; Short and Siegmund, 2019) which also neglects the effects of shear and considers the global in-plane action as the only load transfer mechanism. Also, by virtue of Saint-Venant's principle, we (similarly to the thrust-line model) neglect the effect of stress concentrations near contact regions on the all-important global in-plane deformability.

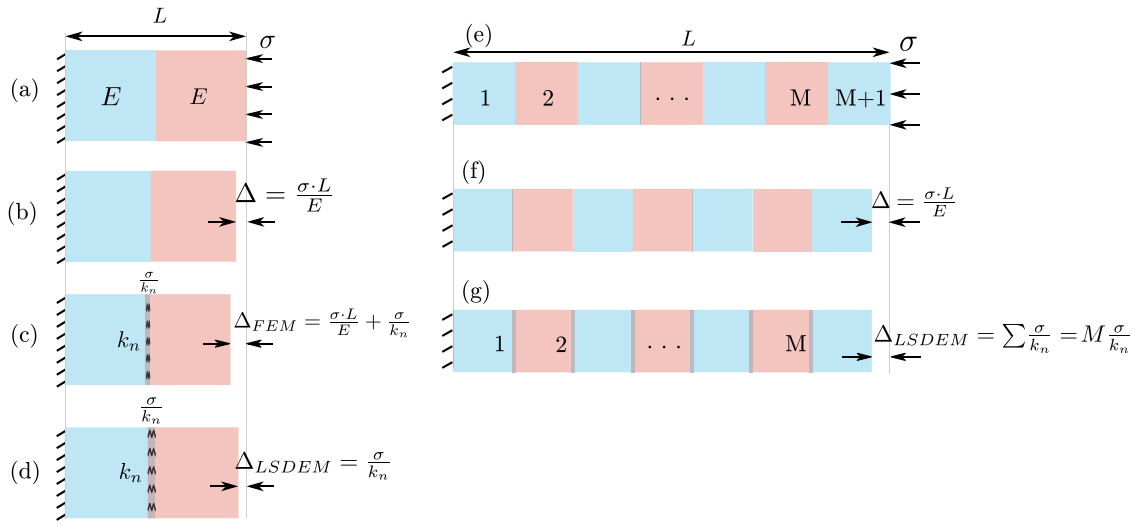

Fig. 3. Methodology — the in-plane deformability is accounted for in LS-DEM through interfacial penetrations: (a–d) a two-block case. (e–g) the multi-block case.

Unlike the penetration stiffness in common FEM/DEM/LS-DEM applications, k_n in Eq. (3) is an explicit correlate of E which requires no calibration. As such, it is considered to be a structural property involving the total number of blocks, the total length, and assuming a common E to all the blocks. Cases involving blocks made of different materials or blocks with significantly different dimensions may require reconsidering k_n as a block-wise property, and are therefore beyond the present scope.

2.4. Limitations

The three main limitations of our model are that (a) it is only applicable to blocks made of relatively rigid materials for which k_n is sufficiently large and the penetrations sufficiently small; soft materials with very small E and k_n may induce too large penetrations that could overly distort the actual (penetration-less) kinematics; (b) it does not account for material non-linearity, specifically fracture, which sometimes plays a role in TIS' failure; and (c) it does not resolve the bulk stresses.[3]

3. Set-up and numerical model

All the numerical examples in this manuscript consider centrally-loaded square TIS panels studied in Mirkhalaf et al. (2019). No experiments were done in this study. This experimental benchmark was chosen because (a) centrally loaded slab-like TIS are the most common TIS studied in the literature; (b) it contains detailed experimental information and ample data for comparison and validation; and (c) the polyhedral blocks used in Mirkhalaf et al. (2019) have planar faces and therefore they interact across matching planes. Such interfaces represent the simplest form of conforming contacts, as distinct from the non-conforming contact typically modeled with discrete element methods. As such, they are a natural starting point for a future investigation of more complex cases of conforming contacts that characterize TIS with curved-face (e.g., osteomorphic) blocks (Dyskin et al., 2003; Djumas et al., 2017, 2016; Estrin et al., 2021).

Fig. 4(a) shows the truncated polyhedral block used in Mirkhalaf et al. (2019) and its xz and yz cross-sections. The bottom face of the blocks is a square with side length l, and the angle of inclination of its sloping lateral faces is θ. Fig. 4(b) shows the basic 5-block cell formed by surrounding a block by four similar ones rotated with respect to it by 90° about the z axis. Fig. 4(c) shows an entire panel with the contour of a basic cell around the central block marked in black. The panels' dimensions are $50 \times 50 \times 3.18$ mm, and they consist of boundary blocks along the edges and internal blocks. The boundary blocks are either halves or quarters (in the four corners) of the internal blocks in a way that the assembled panel's convex hull is a straight parallel-piped.

Panels with identical overall dimensions but with three block sizes – medium, large, and small – are considered. The medium-block panel, depicted in Fig. 4(c), has 5×5 internal blocks with $l = 8.33$ mm, and it is referred to as the 5×5 panel. The large- and small-block panels are referred to, respectively, as the 3×3 and 7×7 panels, see Fig. 4(d).

The panels in Mirkhalaf et al. (2019) were confined by a stiff peripheral frame that held the boundary blocks in place without pre-compression. They were quasi-statically loaded by a pin indenter that pushed the central block in the negative z direction at a rate of 0.01 mm/sec. The force P exerted by the indenter on the panel and the corresponding indenter displacement δ are indicated by a yellow arrow in the -z direction in Fig. 4(c). Fig. 4(e) shows an experimental $P-\delta$ curve, with the main global response parameters indicated in red.

Turning to the LS-DEM model, the blocks were positioned and oriented in the initial undeformed configuration of the panel as illustrated in Fig. 4(c), and the boundary conditions were affected by fixing the boundary blocks. Next, the assembly was subjected to gravity until it reached a relaxed state, i.e., until the kinetic energy lowered to effectively zero. The relaxed positions and rotations of the blocks were then taken as the initial conditions for the main loading phase — the indentation. For the indentation loading, the 2.5 mm spherical tip of the indenter was prescribed a constant velocity in the negative z direction, see Fig. 4(c,d). To expedite the analyses, the loading speed was taken as high as possible, but always low enough to avoid inertial effects. The loading rate values ranged between 3–6 mm/s. The density of the alumina-silicate blocks was taken equal to $2.5 \cdot 10^{-6} \frac{\text{kg}}{\text{mm}^3}$, and a friction coefficient $\mu = 0.23$ was used, in accordance with the data in Mirkhalaf et al. (2019).

Numerical tests detailed in Feldfogel et al. (2022) were carried out to determine the refinement of the surface discretization and of the level-set geometrical representation of the blocks necessary for numerical convergence of the results. The converged surface discretization and Level-set parameters was found to be 0.06 mm and 0.025 mm, and these values were used for all the analyses in this manuscript. Additional computational details are given in Appendix.

[3] Nevertheless, bulk stresses can be estimated at post-processing by solving the continuum problem of blocks loaded by the contact surface tractions which our model provides. This can be done using any continuum model, e.g., FEM.

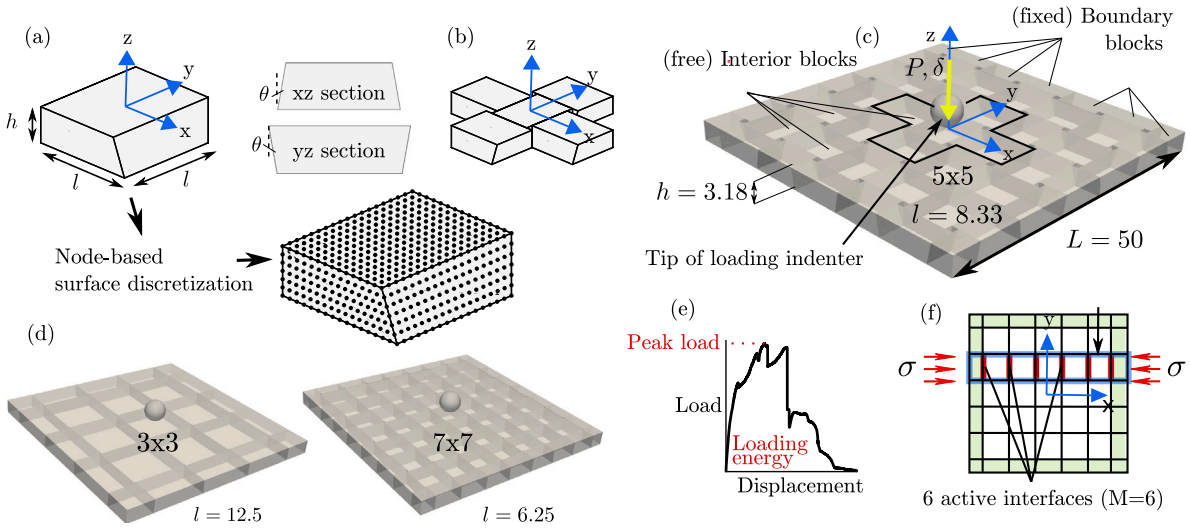

Fig. 4. Configuration — (a) a typical internal block with $\theta = 10°$, its two cross-sections, and its LS-DEM surface discretization; (b) a basic five-block interlocked cell; (c) The full 5×5 panel and its boundary conditions; (d) the 3×3 and 7×7 panels; (e) a typical load displacement curve; and (f) a typical strip to determining k_n^{def} from Eq. (3).

4. Validation

We validate the LS-DEM model in the context of the FEM simulations and experimental results reported in Mirkhalaf et al. (2019). For this, we consider the three cases analyzed in Mirkhalaf et al. (2019) with FEM, namely the 3×3, 5×5, and 7×7 panels with $\theta = 2.5°$. Specifically, we compare the load–deflection response as obtained in FEM and LS-DEM, and examine the latter's ability to capture the experimentally-observed evolution of the failure mechanism, and the internal force chains.

Starting with the ultimate deflection, it is somewhat overestimated by both FEM and the LS-DEM simulations, see Fig. 5(a). LS-DEM is, however, generally closer to the experimental benchmark, especially for the 3×3 panel. Continuing with the peak-load estimates, both LS-DEM and FEM considerably over-estimated the peak load in all three cases, see the specific over-estimation (error) factors in Table 1. To allow comparison of the shape of the load–deflection curves, the FEM and LS-DEM loads were normalized by the over-estimation factors in Table 1 so that they matched the experimental peak-load. The normalized LS-DEM curves in all three cases are a bit closer to the experimental reference compared with the normalized FEM curves. These results show that, in spite of using a fraction of the degrees of freedom, LS-DEM is comparable with FEM in terms of estimating the global response parameters.

Turning to LS-DEM's ability to capture the failure mechanisms, Fig. 5(b) shows that, for all three assemblies, the model captures the failure mechanism observed in the experiments (Mirkhalaf et al., 2019), namely one where the central block gradually slips out of the assembly. In terms of the load transfer mechanism, Fig. 5(c) shows an arch-like internal forces chains in accordance with the thrust-line analogy for slab-like TIS (Khandelwal et al., 2012, 2013; Short and Siegmund, 2019). These results support the physical modeling concepts described in Section 2 and the LS-DEM model in general.

Notwithstanding the ability of LS-DEM to capture the experimentally-observed failure mechanisms and the internal force chains, the ability to estimate the peak load without parameter calibration is far from predictive, see Table 1. As a first step towards better predictive capabilities, we focus in the next section on physical aspects that cause peak-load over-estimates and on heuristic strategies to account for them and thereby to get closer estimates of the structural response.

Table 1
Factors of error of adapted LS-DEM and FEM relative to Mirkhalaf et al. (2019) experiments in the geometrically perfect case.

Response parameter	Assembly index	Overestimation factor	
		FEM (Mirkhalaf et al., 2019)	LS-DEM with k_n^{per}
Peak load [N]	3×3	14–15	7.1
	5×5		3.7
	7×7		3.4
Loading energy [N mm]	3×3	9–13	6.2
	5×5		5.6
	7×7		6.0

5. Two avenues towards improved predictive modeling

5.1. Accounting for initial gaps between the blocks

The over-estimation of the peak load by the FEM simulations was attributed in Mirkhalaf et al. (2019) to the presence of "small gaps between the blocks resulting from statistical variations in the shape of blocks, an effect which has been previously found to significantly affect the mechanical performance in similar materials (Barthelat and Zhu, 2011)". Following this reasoning, with which we concur, we next present and test a simplified modeling approach to account in an approximate way for the effect of gaps.

5.1.1. A simplified approach to accounting for the global effects of gaps

From a structural mechanics perspective, the presence of gaps reduces TIS's global stiffness and carrying capacity because they reduce the in-plane stiffness. Under in-plane compression, the gaps reduce without exerting tractions, leading to total deformation that is always larger than when there are no gaps. Based on the fact that gap reduction and block deformation contribute to the global deformation in-series, we heuristically consider the penetration stiffness in the geometrically imperfect case k_n^{imp} to be a resultant spring of two springs in series — k_n^{def} (which represents the blocks' deformability, see Eq. (3)) and k_n^{gaps} (which represents the contribution of gap closure to the in-plane deformability) thus:

$$k_n = k_n^{imp} = \frac{k_n^{def} \cdot k_n^{gaps}}{k_n^{def} + k_n^{gaps}} \tag{4}$$

In general, the magnitude and distribution of initial gaps is not known a-priori and so there is no close form expression for k_n^{gaps} as the

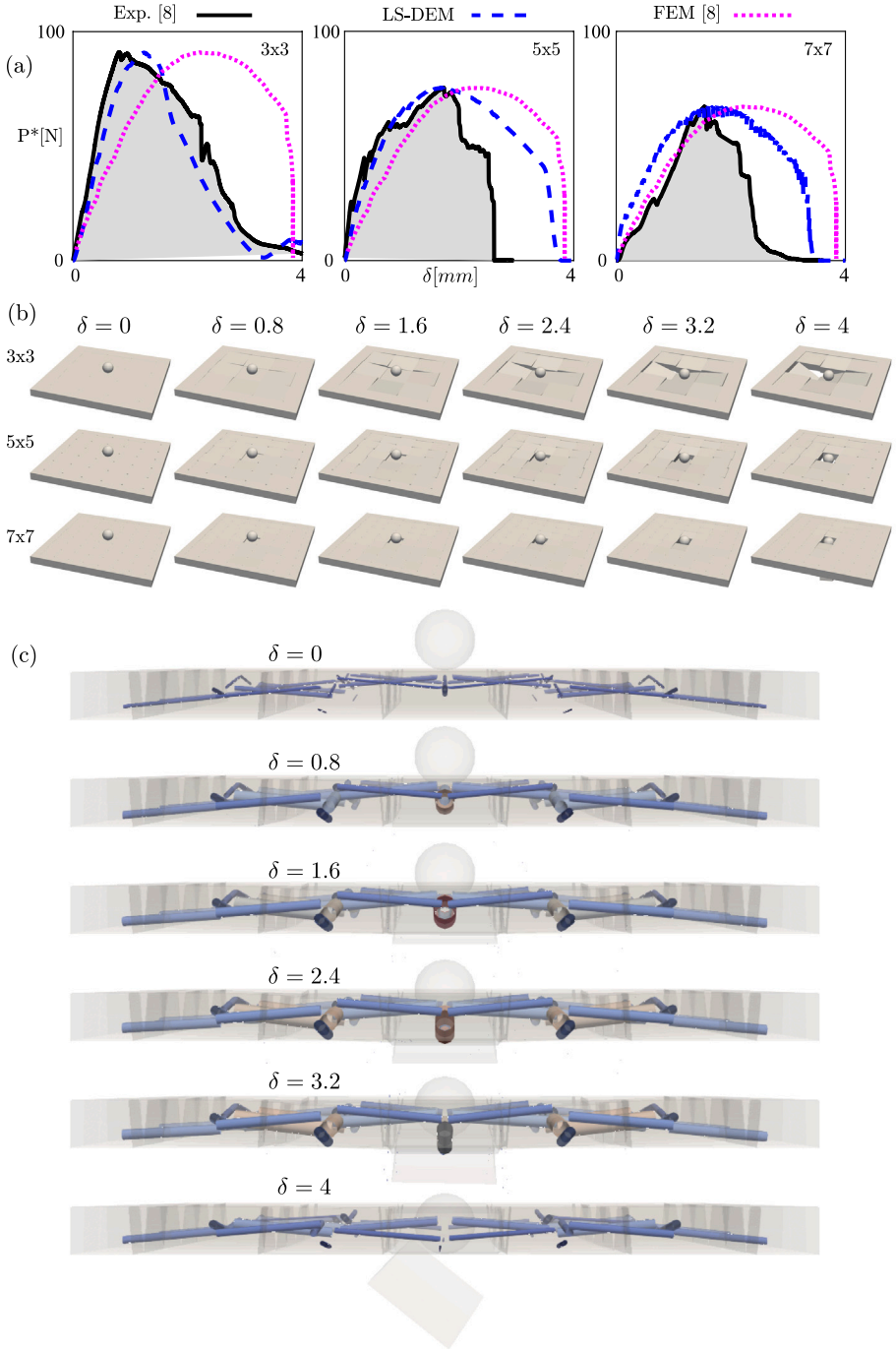

Fig. 5. The performance of the LS-DEM model compared with the experimental and numerical results reported in Mirkhalaf et al. (2019) for the 3 × 3, 5 × 5, and 7 × 7 panels with $\theta = 2.5°$. (a) Load–deflection curves for as obtained from the experiments in Mirkhalaf et al. (2019), the FEM simulations in Mirkhalaf et al. (2019), and the present LS-DEM model. The numerical curves from the FEM and LS-DEM simulations are normalized by the peak experimental load with the normalization (error) factors listed in Table 1. (b) Deformation mode snapshots obtained from the LS-DEM model. (c) The evolution of resultant contact forces for the 5 × 5 panel obtained from the LS-DEM model. The forces directions are represented by the inclination of the cylinders axis and their magnitude is represented by the cylinders width.

one for k_n^{def}. Therefore, when the effect of gaps is taken into account using Eq. (4), the k_n^{gaps} component of k_n^{imp} requires calibration.

5.1.2. Calibration of the gap parameter k_n^{gaps}

We calibrated k_n^{gaps} in the context of the $\theta = 5°$ 5 × 5 panel from Mirkhalaf et al. (2019), keeping k_n^{def} as before at 2.25 GPa/mm. Comparing the experimental and LS-DEM load–deflection curves in Fig. 6, the k_n^{gaps} = 0.49 GPa/mm and k_n^{gaps} = 0.65 GPa/mm curves envelope the experimental one, with the former value closer in terms of peak load, loading energy, and ultimate displacement. Comparing the failure mechanism, the k_n^{gaps} = 0.65 GPa/mm case correctly captures the localized failure observed in the Mirkhalaf et al. (2019) experiments, whereas the k_n^{gaps} = 0.49 GPa/mm case does not. Based on this, we chose the k_n^{gaps} = 0.65 GPa/mm case as the best fit k_n^{gaps}. As an additional check on the validity of the choice of k_n^{gaps} = 0.65 GPa/mm, we plotted the internal force chains obtained with it and found that, similarly to what we found for the closed-form k_n used in Section 4, they are similar to those obtained in FEM simulations (Khandelwal et al., 2012) and are inline with the thrust-line model (Khandelwal et al., 2012, 2013; Short and Siegmund, 2019).

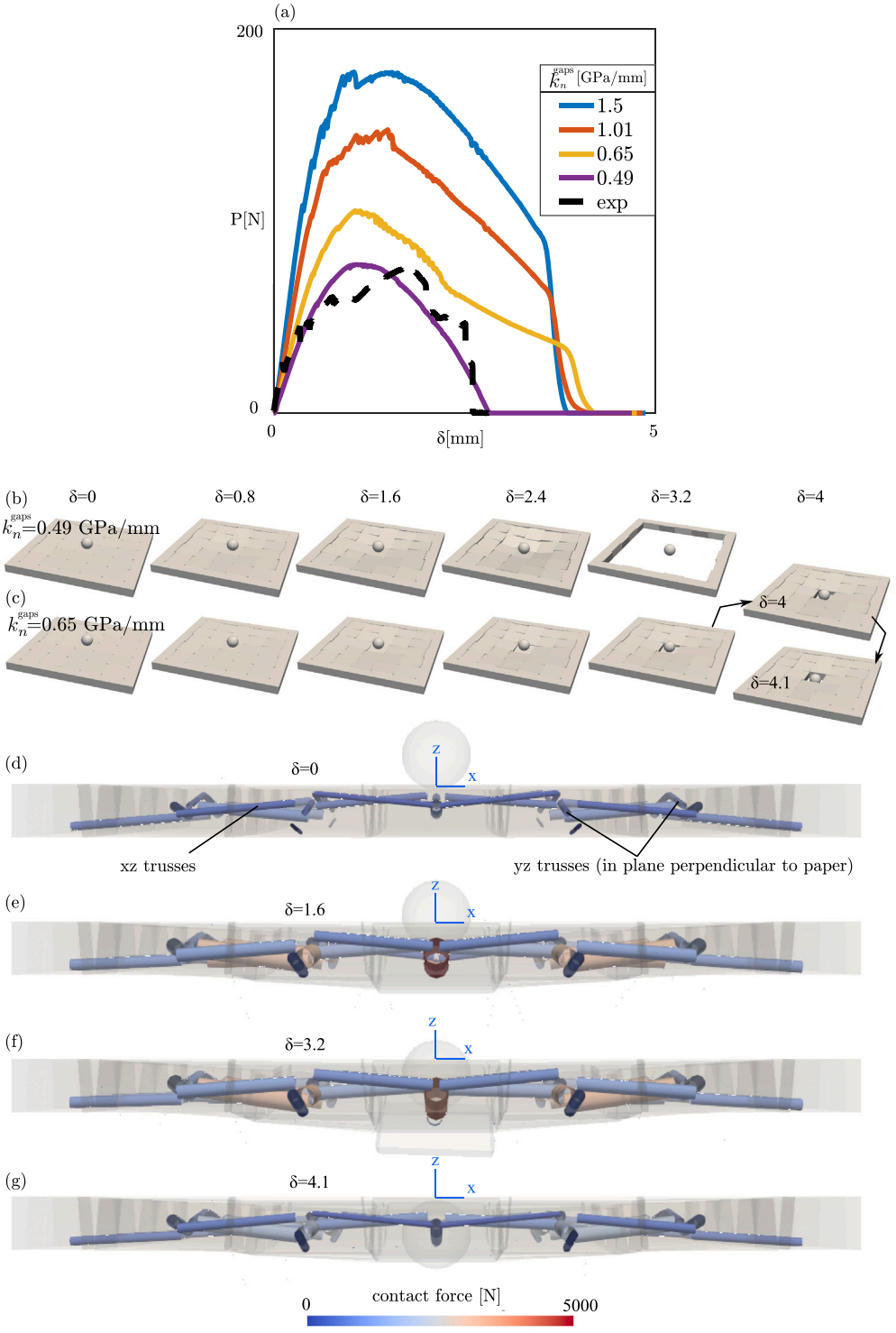

Fig. 6. Calibration of the gap parameter k_n^{gaps}: (a) $P-\delta$ curves of the $\theta = 5°$ 5 × 5 panel with varying k_n^{gaps}; (b–c) failure mechanism snapshots for selected k_n^{gaps}; (d–g) resultant contact forces between the block for k_n^{gaps} = 0.65 GPa/mm at selected δ's, represented by cylinders. The forces direction is represented by the inclination of the cylinders axis and their magnitude is represented by the cylinders width and color. (For interpretation of the references to color in this figure legend, the reader is referred to the web version of this article.)

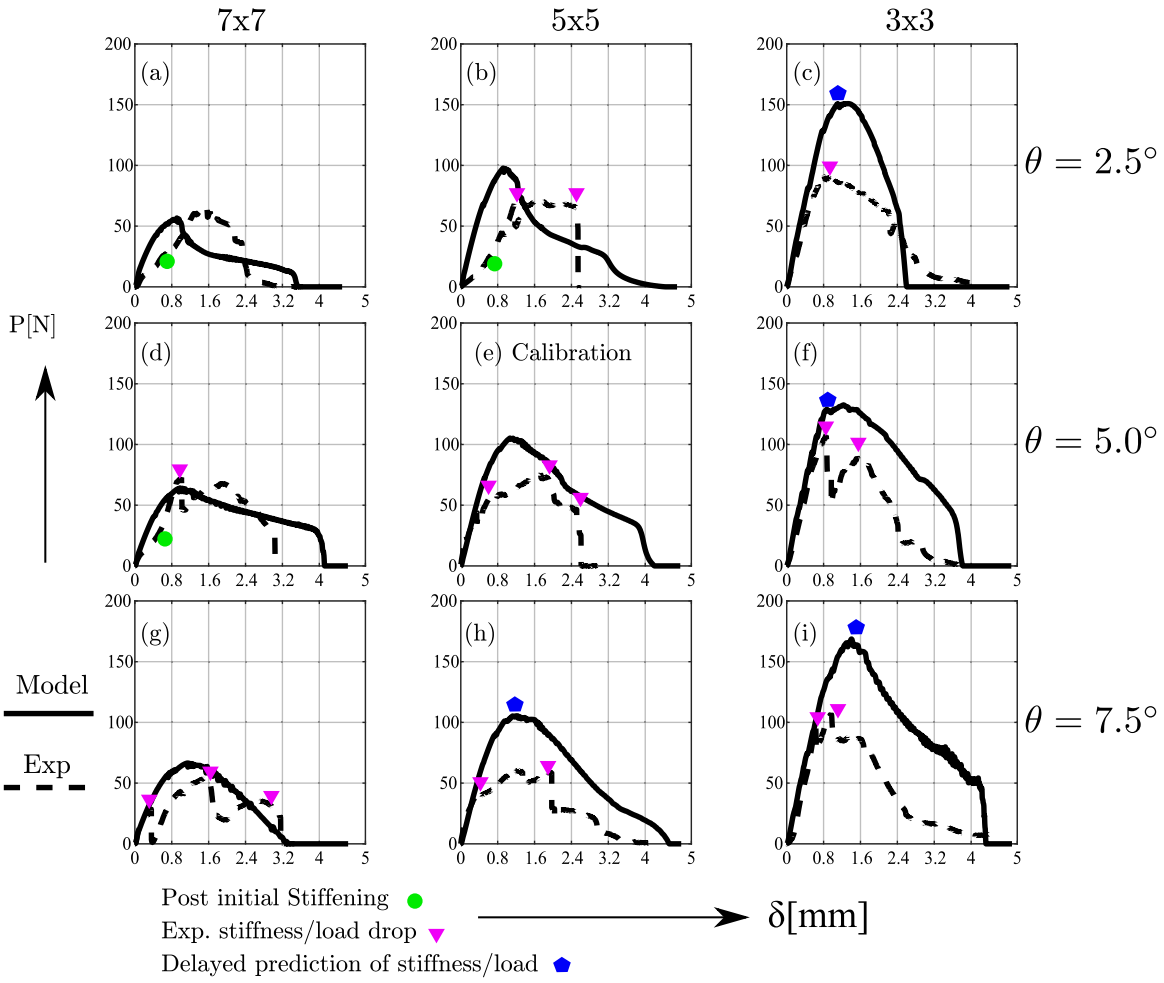

Fig. 7. Comparison between the LS-DEM prediction with calibrated gap parameter to the experimental benchmark results from Mirkhalaf et al. (2019) for the eight test panels (a–d) and (f–i).

5.1.3. Evaluating the validity of k_n^{gaps} and the importance of gaps

To ensure that the calibrated k_n^{gaps} = 0.65 GPa/mm is valid beyond the calibration case, we analyzed with it eight test panels – the remaining combinations of the 3 × 3, 5 × 5, and 7 × 7 panels with $\theta = 2.5°, 5°, 7.5°$ – and compared the results to the experimental benchmark (Mirkhalaf et al., 2019). We used the same k_n^{gaps} for the 3 × 3, 5 × 5, and 7 × 7 panels because, for the same level of geometrical imperfection at the block level, the global effect of gaps is independent of the number of blocks.[4]

Fig. 7 depicts the $P-\delta$ curves of the nine panels, obtained with the calibrated k_n^{gaps} = 0.65 GPa/mm. The error factors for all the cases are summarized in Table 2.

Fig. 7 and Table 2 show that, with the calibrated k_n^{gaps}, the model is quantitatively much closer to the experimental peak load compared with the non-calibrated models, see Table 1. Qualitatively, it captures the increase in peak load and loading energy with block size for all θ's, matches the initial stiffness across the different block sizes and θ's (to a lesser degree in cases a,b,d), captures the negative stiffness phases in (d,f,h,i) and the load drops (c,d,e,f,i) at final stages of failure. In terms of the failure mechanism, with the exception of case (g), the model well captures the experimentally-observed slip-governed failure across the eight test panels. These results show that, even with a very crude approach of accounting for the effects of gaps, the predictive ability of the model is considerably better. They thus support the notion that geometrical imperfection and commensurate initial gaps negatively influence the carrying capacity of TIS and that accounting for them is key to obtaining better predictive capabilities.

Fig. Fig. 8 depicts the failure mechanism for the eight validation cases corresponding to the $P-\delta$ curves in Fig. Fig. 7(a-d,f-i). It shows that, in most cases, the calibrated model correctly captures the experimentally observed slip-governed failure mechanism, with the central block slipping out of the assembly and with some upward rebound Mirkhalaf et al. (2019). Lesser agreement is obtained in cases (c) and (h), where more than one block eventually fall off, and a stick-governed failure different from the experimentally reported one was obtained in case (g).

[4] To see why, consider an imperfection of 0.001 of the side length of the block resulting in a gap of the same magnitude at the block level. For the 3 × 3 block with side length 12.5 mm, this translates to a gap of size 0.0125 mm at the block level, and to a cumulative gap along of 4 × 0.0125 = 0.06 mm (the 3 × 3 has 4 active interfaces). The same calculation for the 7 × 7 panel yields half of the gap at the block level (because the side length is half) but the same cumulative gap (because there are twice the number of interfaces). In other words, the effect of different gaps at the block level on the global in-plane deformability is exactly off-set by the number of interfaces such that the effect of gaps is independent of the number of blocks.

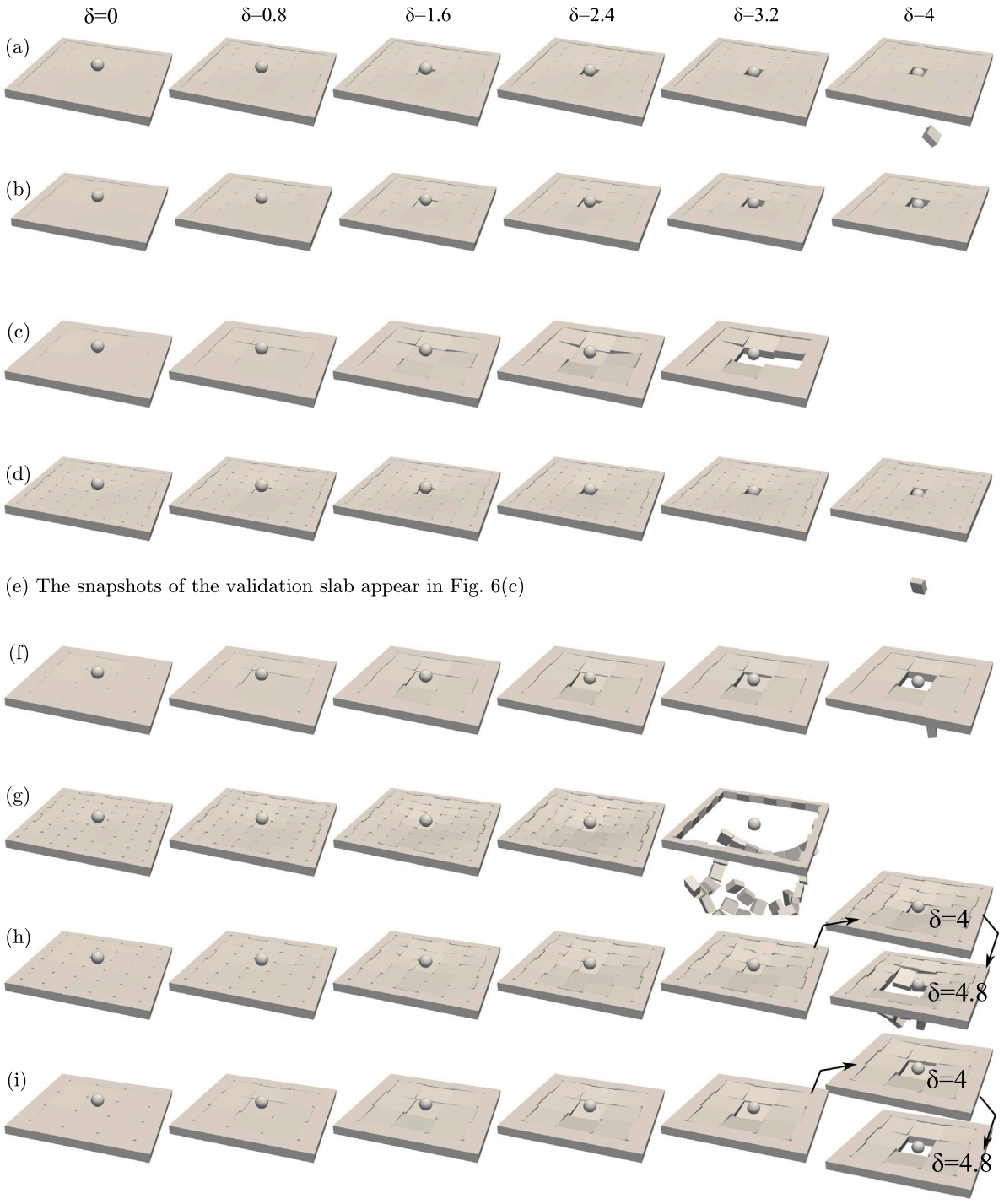

Fig. 8. Failure mechanism snapshots of the eight validation panels.

We note that the better quantitative agreement of the calibrated model compared with the non-calibrated FEM and LS-DEM models comes at the expense of performing a problem-specific set of initial analyses to calibrate k_n^{gaps}, which is a disadvantage for a predictive model. Also, the quantitative agreement of the calibrated model for different TIS configurations may be better or worse then that reflected in Fig. 7 and Table 2. This, together with the fact that our simple approach only accounts for the effects of gaps in a global and approximate sense, points to the need for more in-depth studies on the effects of gaps in various TIS configurations.

5.2. Accounting for 'Second-order' effects

5.2.1. Additional, non-gap-related, causes for model-experiment discrepancies

Notwithstanding the closer estimates of the structural response when the effects of gaps are accounted for (see Fig. 7 and Table 2), there are still noticeable discrepancies between the experimental results and the model predictions. These can be attributed to the compliance of the peripheral boundary element and small in-plane slipping failures between the peripheral element and the boundary blocks, factors not

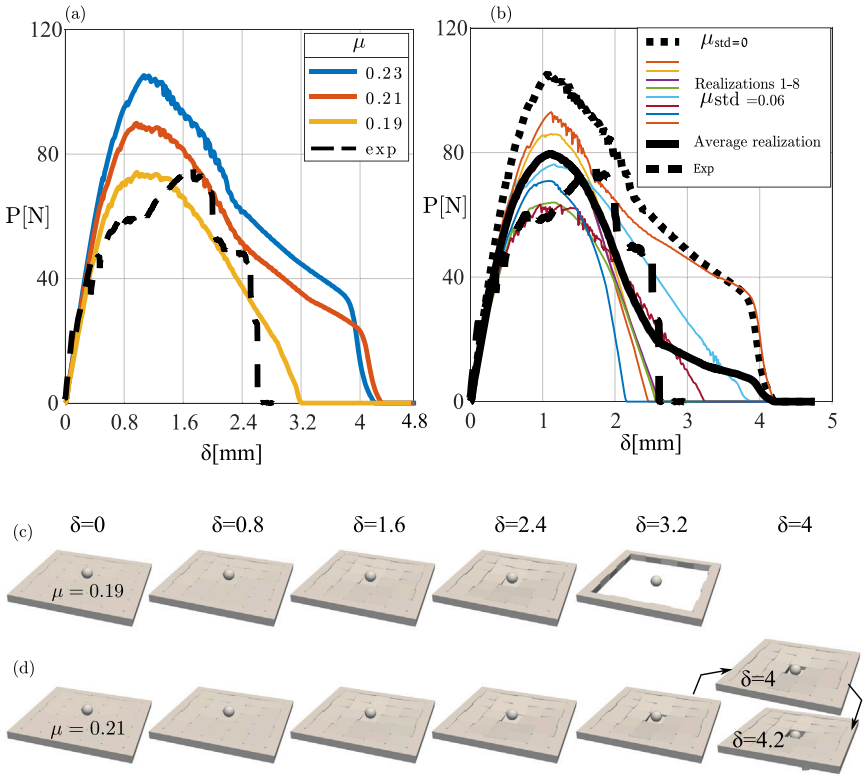

Fig. 9. The discrepancies between analyses and experiment can be reduced by simple modifications in the friction model: (a) $P-\delta$ curves with smaller-than-nominal μ's; (b) $P-\delta$ curves from 8 realizations with randomly generated μ's; (c,d) failure mechanism snapshots for selected μ's. (For interpretation of the references to color in this figure legend, the reader is referred to the web version of this article.)

Table 2
Error factors in validation of calibrated model — the errors are smaller than FEM's by an order of magnitude, reasonable in absolute terms, and similar in the calibration panel and the validation panels, supporting the model's validity.

Assembly	$\theta°$	$P^{exp}_{max}/P^{model}_{max}$	$LE^{exp}_{max}/LE^{model}_{max}$
7 × 7		0.85	1.02
5 × 5	2.5	1.36	1.42
3 × 3		1.66	1.44
7 × 7		0.88	1.25
5 × 5	5	**1.40**	**1.84**
3 × 3		1.74	2.13
7 × 7		1.24	1.92
5 × 5	7.5	1.21	1.37
3 × 3		1.58	2.22
Average error factors		**1.32**	**1.62**
Standard deviation		0.32	0.42
Standard deviation [%]		24	26

accounted for in our model. Such factors may explain the markedly smaller initial stiffness and unexplained stiffening in cases (a,b,d), indicated by green circles in Fig. 7. This reasoning is supported by the fact that good agreement with the experiments was obtained in cases (c),(e),(f),(g, after the initial early load drop), (h) and (i), and that in all of these cases the variations in the (experimental) initial stiffness were relatively small.

In addition to the discrepancies discussed in the preceding paragraph, we see in Fig. 7 that, in the LS-DEM model, the load/stiffness drops that follow the initial linear response (and which are indicated by blue five-point stars in the figure) always occur later than in the experimental curves, which explains the general overestimation of the peak-load, even when the effects of gaps are taken into account. We attribute the delayed stiffness/load drop transition of the model to friction-related factors like frictional instabilities and to friction strength variability, factors which simplistic friction models such as a bi-linear Coulomb's law (to our knowledge, the only one hitherto used in the TIS literature) do not account for. That such factors play a role in TIS' structural response is suggested by the sharp, and otherwise unexplained load/stiffness drops in Fig. 7(d–i). Next, we examine the possible effects of friction-related factors using simple approximate strategies to account for their effects.

5.2.2. *The effects of friction-related instability and variability*

The effect of friction-instabilities-induced load drop upon sliding initiation can be roughly approximated by assuming smaller friction coefficients than the nominal one. The effects of μ variability can be examined by attributing a random distribution of friction coefficients to the blocks. Fig. 9(a) shows that smaller friction coefficients are in a closer agreement with the experimental curve. However, while the failure mechanism for the $\mu = 0.21$ remains correct, see Fig. 9(d), the better $P-\delta$ agreement with $\mu = 0.19$ comes at the expense of losing the correct failure mechanism, see Fig. 9(c).

Fig. 9(b) illustrates the effect of introducing μ variability to the model. The eight thin colored lines correspond to eight realizations of the model wherein the μ's for the different blocks were obtained randomly from a normal distribution with mean 0.23 (the nominal value) and standard deviation (std) 0.06. It can be seen that the average realization enveloped by the eight realizations is much closer to the experimental benchmark than the reference analysis with deterministic $\mu = 0.23$.

Fig. 9(a,b) suggests that friction-related effects may play an important in the structural response of TIS. This points to the need to better understand and study them on the one hand, and to the improved predictive power gained by accounting for them in models on the other.

6. Conclusion

We have presented a new modeling approach for topologically interlocked structures, based on the Level-Set-Discrete-Element-Method. This approach aims at facing the modeling challenges posed by the unique behavior and failure of these structures within a Discrete Element framework, as an alternative to the commonly-used FEM approach.

After outlining the theoretical basis of our approach, we have shown that, without parameter calibration, our model can capture the experimentally-observed slip-governed failure mechanisms and the arch-like internal load transmission paths in centrally-loaded slab-like TIS. Next, in an attempt to identify paths towards more predictive modeling, we applied the new model to explore the effects of initial gaps and friction-related phenomena on TIS structural response, described simple modeling concepts to account for them, and showed that this improved the agreement with experimental benchmarks.

The theoretical basis and the ability of our model to describe and quantify the behavior of topologically interlocked structures establish an initial proof-of-concept of our new Level-Set-DEM approach. Future research will focus on further examining the validity of our new approach in different TIS configurations and on refining the work towards calibration-free and predictive computational models.

CRediT authorship contribution statement

Shai Feldfogel: Conceptualization, Methodology, Software, Validation, Formal analysis, Writing – original draft. **Konstantinos Karapiperis:** Methodology, Software, Writing – review & editing. **Jose Andrade:** Methodology, Writing – review & editing. **David S. Kammer:** Conceptualization, Methodology, Resources, Writing – review & editing.

Declaration of competing interest

The authors declare that they have no known competing financial interests or personal relationships that could have appeared to influence the work reported in this paper.

Data availability

The simulation data generated in this study have been deposited in the ETH Research Collection database.

Acknowledgments

Shai Feldfogel was a Swiss Government Excellence Scholarship holder for the academic years 2021–2022 (ESKAS No. 2021.0165).

Appendix. Computational information

The c++ LS-DEM code used for the analyses in this manuscript was run on the ETH Euler cluster. A typical analysis of the 5×5 assembly (49 blocks + the spherical indenter tip) with the most refined surface discretization with a distance of 0.06 mm between surface nodes took approximately 50 CPU hours to run, without parallelization and code optimization. The preprocessing stage, where the Level-Set geometrical representations of the blocks are calculated, and which only has to be done once per structure, took about 8 h. The 100,000 time-increments of the relaxation under gravity took about 7 h, and the 500,000 time-increments of indentation loading took about 35 h. The time step Δt_{LSDEM} required for numerical stability of the explicit formulation was about 1 ms. Analyses with less refined discretizations that yielded results fairly close to the converged ones took only a few hours.

References

Barthelat, F., Zhu, D., 2011. A novel biomimetic material duplicating the structure and mechanics of natural nacre. J. Mater. Res. 26 (10), 1203–1215. http://dx.doi.org/10.1557/jmr.2011.65, https://www.cambridge.org/core/journals/journal-of-materials-research/article/novel-biomimetic-material-duplicating-the-structure-and-mechanics-of-natural-nacre/D682493DE59E6882B4888E45D2676481, ISSN: 2044-5326, 0884-2914.

Brugger, C., Bréchet, Y., Fivel, M., 2008. Experiments and numerical simulations of interlocked materials. Adv. Mater. Res. (ISSN: 1662-8985) 47–50, 125–128. http://dx.doi.org/10.4028/www.scientific.net/AMR.47-50.125, https://www.scientific.net/AMR.47-50.125.

Brugger, C., Fivel, M.C., Brechet, Y., 2009. Numerical simulations of topologically interlocked materials coupling DEM methods and FEM calculations: Comparison with indentation experiments. MRS Online Proc. Libr. (ISSN: 1946-4274) 1188 (1), 106–111. http://dx.doi.org/10.1557/PROC-1188-LL05-05.

Carlesso, M., Giacomelli, R., Krause, T., Molotnikov, A., Koch, D., Kroll, S., Tushtev, K., Estrin, Y., Rezwan, K., 2013. Improvement of sound absorption and flexural compliance of porous alumina-mullite ceramics by engineering the microstructure and segmentation into topologically interlocked blocks. J. Eur. Ceram. Soc. (ISSN: 0955-2219) 33 (13), 2549–2558. http://dx.doi.org/10.1016/j.jeurceramsoc.2013.05.006, https://www.sciencedirect.com/science/article/pii/S0955221913002458.

Carlesso, M., Molotnikov, A., Krause, T., Tushtev, K., Kroll, S., Rezwan, K., Estrin, Y., 2012. Enhancement of sound absorption properties using topologically interlocked elements. Scr. Mater. (ISSN: 1359-6462) 66 (7), 483–486. http://dx.doi.org/10.1016/j.scriptamat.2011.12.022, https://www.sciencedirect.com/science/article/pii/S1359646211007706.

Cundall, P.A., Strack, O.D.L., 1979. A discrete numerical model for granular assemblies. Géotechnique (ISSN: 0016-8505) 29 (1), 47–65. http://dx.doi.org/10.1680/geot.1979.29.1.47, https://www.icevirtuallibrary.com/doi/abs/10.1680/geot.1979.29.1.47.

Dalaq, A.S., Barthelat, F., 2019. Strength and stability in architectured spine-like segmented structures. Int. J. Solids Struct. (ISSN: 0020-7683) 171, 146–157. http://dx.doi.org/10.1016/j.ijsolstr.2019.04.012, https://www.sciencedirect.com/science/article/pii/S0020768319301829.

Dalaq, A.S., Barthelat, F., 2020. Manipulating the geometry of architectured beams for maximum toughness and strength. Mater. Des. (ISSN: 0264-1275) 194, 108889. http://dx.doi.org/10.1016/j.matdes.2020.108889, https://www.sciencedirect.com/science/article/pii/S0264127520304238.

Djumas, L., Molotnikov, A., Simon, G.P., Estrin, Y., 2016. Enhanced mechanical performance of bio-inspired hybrid structures utilising topological interlocking geometry. Sci. Rep. (ISSN: 2045-2322) 6 (1), 26706. http://dx.doi.org/10.1038/srep26706, https://www.nature.com/articles/srep26706.

Djumas, L., Simon, G.P., Estrin, Y., Molotnikov, A., 2017. Deformation mechanics of non-planar topologically interlocked assemblies with structural hierarchy and varying geometry. Sci. Rep. (ISSN: 2045-2322) 7 (1), 11844. http://dx.doi.org/10.1038/s41598-017-12147-3, https://www.nature.com/articles/s41598-017-12147-3.

Dyskin, A.V., Estrin, Y., Pasternak, E., 2019. Topological interlocking materials. In: Architectured Materials in Nature and Engineering: Archimats. In: Springer Series in Materials Science, Cham, ISBN: 978-3-030-11942-3, pp. 23–49, https://doi.org/10.1007/978-3-030-11942-3_2.

Dyskin, A., Estrin, Y., Pasternak, E., Khor, H., Kanel-Belov, A., 2003. Fracture resistant structures based on topological interlocking with non-planar contacts. Adv. Eng. Mater. (ISSN: 1527-2648) 5 (3), 116–119. http://dx.doi.org/10.1002/adem.200390016, https://onlinelibrary.wiley.com/doi/abs/10.1002/adem.200390016.

Dyskin, A.V., Estrin, Y., Pasternak, E., Khor, H.C., Kanel-Belov, A.J., 2005. The principle of topological interlocking in extraterrestrial construction. Acta Astronaut. (ISSN: 0094-5765) 57 (1), 10–21. http://dx.doi.org/10.1016/j.actaastro.2004.12.005, https://www.sciencedirect.com/science/article/pii/S0094576504004084.

Dyskin, A.V., Pasternak, E., Estrin, Y., 2012. Mortarless structures based on topological interlocking. Front. Struct. Civ. Eng. (ISSN: 1673-7512) 6 (2), 188–197. http://dx.doi.org/10.1007/s11709-012-0156-8, https://link.springer.com/article/10.1007/s11709-012-0156-8.

Estrin, Y., Krishnamurthy, V.R., Akleman, E., 2021. Design of architectured materials based on topological and geometrical interlocking. J. Mater. Res. Technol. (ISSN: 2238-7854) 15, 1165–1178. http://dx.doi.org/10.1016/j.jmrt.2021.08.064, https://www.sciencedirect.com/science/article/pii/S2238785421008899.

Feldfogel, S., Karapiperis, K., Andrade, J., Kammer, D.S., 2022. A discretization-convergent Level-Set-DEM. arXiv preprint arXiv:2209.15431.

Feng, Y., Siegmund, T., Habtour, E., Riddick, J., 2015. Impact mechanics of topologically interlocked material assemblies. Int. J. Impact Eng. (ISSN: 0734-743X) 75, 140–149. http://dx.doi.org/10.1016/j.ijimpeng.2014.08.003, https://www.sciencedirect.com/science/article/pii/S0734743X14001821.

Karapiperis, K., Monfared, S., Macedo, R.B.d., Richardson, S., Andrade, J.E., 2022. Stress transmission in entangled granular structures. Granul. Matter (ISSN: 1434-7636) 24 (3), 91. http://dx.doi.org/10.1007/s10035-022-01252-4.

Kawamoto, R., Andò, E., Viggiani, G., Andrade, J.E., 2016. Level set discrete element method for three-dimensional computations with triaxial case study. J. Mech. Phys. Solids (ISSN: 0022-5096) 91, 1–13. http://dx.doi.org/10.1016/j.jmps.2016.02.021, https://www.sciencedirect.com/science/article/pii/S002250961530154X.

Khandelwal, S., Siegmund, T., Cipra, R.J., Bolton, J.S., 2012. Transverse loading of cellular topologically interlocked materials. Int. J. Solids Struct. (ISSN: 0020-7683) 49 (18), 2394–2403. http://dx.doi.org/10.1016/j.ijsolstr.2012.04.035, https://www.sciencedirect.com/science/article/pii/S0020768312001886.

Khandelwal, S., Siegmund, T., Cipra, R.J., Bolton, J.S., 2013. Scaling of the elastic behavior of two-dimensional topologically interlocked materials under transverse loading. J. Appl. Mech. (ISSN: 0021-8936) 81 (3), http://dx.doi.org/10.1115/1.4024907.

Koureas, I., Pundir, M., Feldfogel, S., Kammer, D.S., 2022. On the failure of beam-like topologically interlocked structures. Int. J. Solids Struct. 259, 112029, Publisher: Elsevier.

Krause, T., Molotnikov, A., Carlesso, M., Rente, J., Rezwan, K., Estrin, Y., Koch, D., 2012. Mechanical properties of topologically interlocked structures with elements produced by freeze gelation of ceramic slurries. Adv. Eng. Mater. (ISSN: 1527-2648) 14 (5), 335–341. http://dx.doi.org/10.1002/adem.201100244.

Mirkhalaf, M., Sunesara, A., Ashrafi, B., Barthelat, F., 2019. Toughness by segmentation: Fabrication, testing and micromechanics of architectured ceramic panels for impact applications. Int. J. Solids Struct. (ISSN: 0020-7683) 158, 52–65. http://dx.doi.org/10.1016/j.ijsolstr.2018.08.025, https://www.sciencedirect.com/science/article/pii/S0020768318303433.

Molotnikov, A., Estrin, Y., Dyskin, A.V., Pasternak, E., Kanel-Belov, A.J., 2007. Percolation mechanism of failure of a planar assembly of interlocked osteomorphic elements. Eng. Fract. Mech. (ISSN: 0013-7944) 74 (8), 1222–1232. http://dx.doi.org/10.1016/j.engfracmech.2006.07.012, https://www.sciencedirect.com/science/article/pii/S0013794406002785.

Rezaee Javan, A., Seifi, H., Xu, S., Ruan, D., Xie, Y.M., 2017. The impact behaviour of plate-like assemblies made of new interlocking bricks: An experimental study. Mater. Des. (ISSN: 0264-1275) 134, 361–373. http://dx.doi.org/10.1016/j.matdes.2017.08.056, https://www.sciencedirect.com/science/article/pii/S0264127517308146.

Schaare, S., Dyskin, A.V., Estrin, Y., Arndt, S., Pasternak, E., Kanel-Belov, A., 2008. Point loading of assemblies of interlocked cube-shaped elements. Internat. J. Engrg. Sci. (ISSN: 0020-7225) 46 (12), 1228–1238. http://dx.doi.org/10.1016/j.ijengsci.2008.06.012, https://www.sciencedirect.com/science/article/pii/S0020722508001079.

Short, M., Siegmund, T., 2019. Scaling, growth, and size effects on the mechanical behavior of a topologically interlocking material based on tetrahedra elements. J. Appl. Mech. (ISSN: 0021-8936) 86 (11), http://dx.doi.org/10.1115/1.4044025.

Williams, A., Siegmund, T., 2021. Mechanics of topologically interlocked material systems under point load: Archimedean and Laves tiling. Int. J. Mech. Sci. (ISSN: 0020-7403) 190, 106016. http://dx.doi.org/10.1016/j.ijmecsci.2020.106016, https://www.sciencedirect.com/science/article/pii/S0020740320315290.